



SUSTAIN Deliverable

D5.2 Characterization of TEGs in the lab and across the building

Grant Agreement number	101071179
Action Acronym	SUSTAIN
Action Title	Smart Building Sensitive to Daily Sentiment
Type of action:	HORIZON EIC Grants
Version date of the Annex I against which the assessment will be made	28 th March 2022
Start date of the project	1 st October 2022
Due date of the deliverable	M24
Actual date of submission	30 th September 2024
Lead beneficiary for the deliverable	UPC
Dissemination level of the deliverable	Restricted

Action coordinator's scientific representative

Prof. Stephan Sigg
AALTO –KORKEAKOULUSÄÄTIÖ,
Aalto University School of Electrical Engineering, Department of Communications and Networking
stephan.sigg@aalto.fi



Funded by the European Union. Views and opinions expressed are however those of the author(s) only and do not necessarily reflect those of the European Union or European Innovation Council and SMEs Executive Agency (EISMEA). Neither the European Union nor the granting authority can be held responsible for them.



Name	Beneficiary	e-mail
Ridwan, Mohamad	UPC	mohamad.ridwan@upc.edu
Reverter, Ferran	UPC	ferran.reverter@upc.edu
Gasulla, Manel	UPC	manel.gasulla@upc.edu

Abstract

This deliverable, D5.2, summarizes the work conducted in Task 5.2 of Work Package 5 (WP5) of the SUSTAIN project. The goal of WP5 is to power the sensor nodes developed within the SUSTAIN project through energy harvesting from three different sources: light, thermal, and radiofrequency. Task 5.2 specifically focuses on thermal energy harvesting, which presents challenges due to the relatively low thermal gradient and it cannot be guaranteed to exist all the time.

The primary objectives of Task 5.2 are to characterize thermoelectric generators (TEGs) both in the laboratory and throughout a building. For practical reasons, the chosen building is the Castelldefels School of Telecommunications and Aerospace Engineering (EETAC) at the Universitat Politècnica de Catalunya (UPC). The work has been divided into three main parts:

1. Temperature measurement of heat and cold sources across the building.
2. Laboratory characterization of commercial TEGs using a thermal plate.
3. In situ characterization of TEGs and their energy output.

The document is organized according to these parts, and each section provides an introduction, a description of the materials and methods used, and the experimental results obtained, followed by a discussion. The ultimate goal is to identify the most suitable TEG technologies for various scenarios, depending on the location and type of thermal source.

Contents

1	Introduction.....	3
1.1	Thermoelectric Generators (TEGs).....	3
1.2	Organization and Objectives	5
2	Temperature measurement of heat and cold sources across the building	7
2.1	Introduction.....	7
2.2	Materials and Methods	7
2.3	Experimental Results and Discussion	9
3	Laboratory characterization of commercial TEGs using a thermal plate	12
3.1	Introduction.....	12
3.2	Materials and Methods	12
3.3	Experimental Results and Discussion	16
4	In-situ building characterization of TEGs and their electrical energy output.....	23
4.1	Introduction.....	23
4.2	Materials and Methods	24
4.3	Experimental Results and Discussion	25
5	Conclusions.....	28
6	References	29

1 Introduction

In the era of the Internet of Things (IoT), the deployment of sensor nodes has become ubiquitous across various domains, including smart buildings, industrial automation, and environmental monitoring [1]. These sensor nodes play a crucial role in collecting and transmitting data, enabling real-time decision-making and automation. The proliferation of IoT devices is expected to increase exponentially, with projections indicating that these sensors will be deployed in indoor environments in the near future [2]. Indoor energy harvesting offers a sustainable and eco-friendly solution for powering low-energy devices within buildings. Many applications, including portable consumer electronics and wireless sensors for the IoT, demand a reliable, cost-effective, lightweight, and compact energy source that can provide adequate power under diverse conditions, whether indoors or outdoors [3].

One of the significant challenges in the deployment of IoT sensor nodes is the sustainable powering of these devices. Traditionally, batteries have been the predominant power source for such sensor nodes. However, batteries possess several inherent limitations. They have a finite energy capacity, requiring frequent replacements or recharging, which increases maintenance efforts and costs. Additionally, the production, usage, and disposal of batteries have significant environmental impacts, contributing to pollution and resource depletion. Therefore, finding alternative, sustainable power sources for IoT devices is critical for the widespread adoption and long-term viability of IoT technologies [4]. To address these challenges, there is growing interest in developing autonomous power solutions by harnessing energy from the ambient environment. This approach leverages various energy sources such as sunlight [5], mechanical vibrations [6], radio frequency (RF) signals [7], and thermal gradients [8]. This study is focused on thermal energy harvesting, which employs Thermoelectric Generators (TEGs).

1.1 Thermoelectric Generators (TEGs)

TEGs are solid-state devices that generate electrical power through the Seebeck effect [9]. The Seebeck effect describes the generation of an electric potential across a thermoelectric material when it is exposed to a temperature gradient between its hot and cold sides. The output voltage generated by a TEG can be expressed as

$$V_{OC} = S \Delta T_{TEG} \quad (1)$$

where V_{OC} is the output voltage of a TEG, S is the Seebeck coefficient and ΔT_{TEG} is the temperature differential across the TEG.

TEGs are composed of p-type and n-type semiconductor materials, as shown in Fig. 1a, connected electrically in series and thermally in parallel, enabling the conversion of thermal energy into electrical energy. Hot side is connected to the thermal source and a heatsink is connected to the cold side to improve the heat flow and thus increase ΔT_{TEG} . Recent advancements in materials science have led to the development of more efficient thermoelectric materials, improving the viability of TEGs for low-grade heat harvesting [9]. A TEG can be electrically modelled as an equivalent Thévenin, i.e. a voltage source V_{oc} in series with an internal resistance (R_{in}). Fig. 1b shows this model with a connected output load (R_L), where V_o and I_o are the output voltage and current, respectively. Thus, the power over R_L can be expressed as

$$P_o = \frac{V_{OC}^2}{(R_{in} + R_L)^2} R_L = \frac{S^2 (\Delta T_{TEG})^2}{(R_{in} + R_L)^2} R_L \quad (2)$$

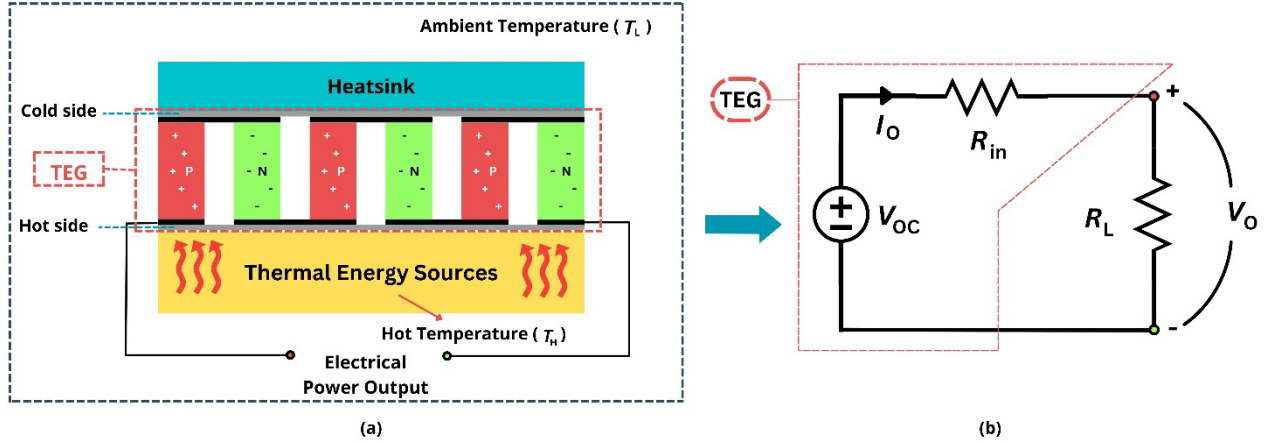


Figure 1. (a) TEG structure and (b) electrical model with a connected output load (R_L)

As can be seen, P_o is directly proportional to the square of ΔT_{TEG} .

TEGs must operate at its maximum power point (MPP) in order to harness the maximum available energy, which happens when $V_o = V_{oc}/2$ [10], i.e. when $R_L = R_{in}$. Thus, from (2), the MPP power (P_{MPP}) is given by

$$P_{MPP} = \frac{V_{OC}^2}{4R_L} = \frac{S^2 (\Delta T_{TEG})^2}{4R_L} \quad (3)$$

Fig. 2 illustrates the ideal graphs I_o - V_o and P_o - V_o . In the second graph, P_{MPP} is marked.

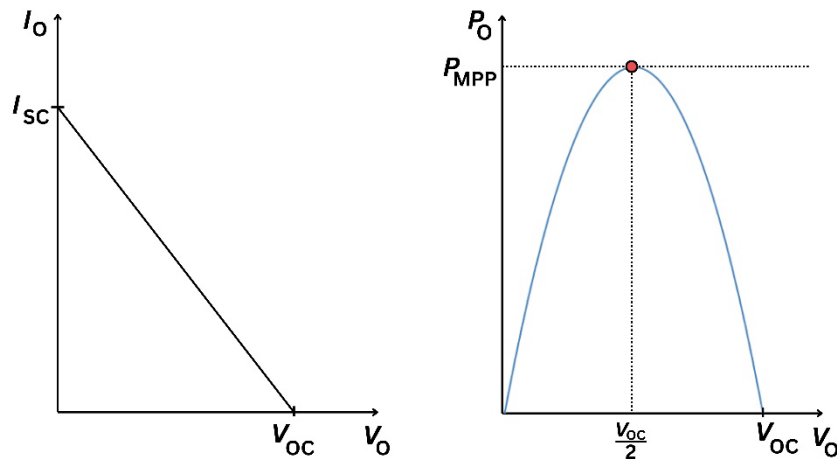


Figure 2. Ideal output current and power versus voltage graphs of a TEG.

In order to increase ΔT_{TEG} , a heatsink must be attached to the cold side. Fig. 3 illustrates this together with the electrical equivalent circuit used for thermal analysis, where R_{TEG} , R_{HS} , and R_{TIM} are the thermal resistances of the TEG, heatsink, and interface material, respectively.

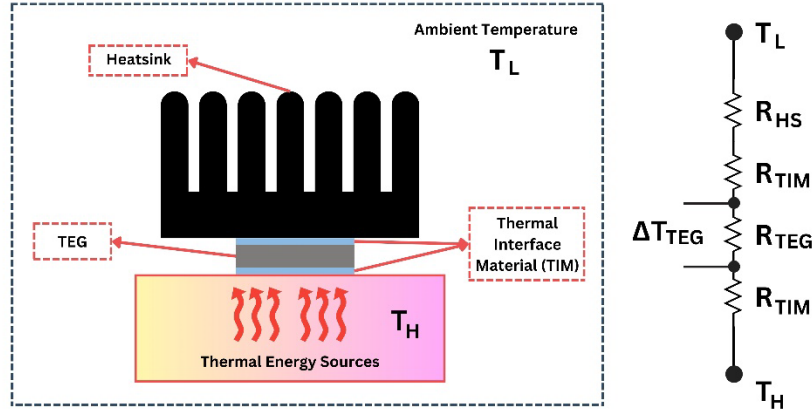


Figure 3. TEG disposal between the thermal source and the heatsink and corresponding electrical equivalent circuit for thermal analysis

The heat flow is given by

$$Q = \frac{T_H - T_L}{R_T} \quad (4)$$

where T_H and T_L are the thermal source and ambient temperatures, respectively, and

$$R_T = R_{TEG} + R_{HS} + 2R_{TIM} \quad (5)$$

Thus,

$$\Delta T_{TEG} = \left(\frac{R_{TEG}}{R_T} \right) \Delta T \quad (6)$$

where $\Delta T = T_H - T_L$. So, in order to maximize ΔT_{TEG} , R_{HS} and R_{TIM} should be as low as possible. Increasing the heat dissipation area of the heatsink can effectively reduce R_{HS} [11].

TEG devices generally operate by employing a heat source that is warmer (T_H) than the surrounding environment (T_L), utilizing the ambient as a "cooler" to facilitate outward heat transfer, which is subsequently absorbed by the ambient. In this scenario, the focus is mainly on recovering energy that is being wasted by the heat source. Thermal energy harvesting also takes place when the an object is at a lower temperature than the surrounding environment, leading to an energy transfer from the ambient to the object, thereby resulting in a net energy loss from the ambient [8]. Indoor environments offer unique opportunities for harnessing waste heat from various sources such as lighting, electronic devices, and hot/cold piping systems. For instance, fluorescent lamps generate localized heat that can be exploited for energy harvesting. By strategically placing TEGs in locations with consistent temperature differentials, it could be possible to generate sufficient electrical power to sustain IoT sensor nodes.

1.2 Organization and Objectives

This study, as part of the SUSTAIN project's Work Package 5 (WP5), focuses on the feasibility and limitations of utilizing TEGs for indoor applications. The specific objectives are: (1) Temperature measurement of heat

and cold sources across the building, (2) Laboratory characterization of commercial TEGs using a thermal plate, and (3) In situ characterization of TEGs and their electrical energy output.

The first objective focuses on thermal measurement across the building to identify potential thermal energy sources. This involves conducting a thorough thermal survey of the building to map out areas with significant thermal sources. The survey includes measuring temperatures around heating/cooling systems, electronic devices, lighting fixtures, and other potential sources of waste heat. The goal is to locate and quantify thermal hot and cold spots where TEGs can be effectively deployed. This data will inform the strategic placement of TEGs to maximize energy harvesting potential, ensuring that the most promising locations are utilized.

The second objective, laboratory characterization of commercial TEGs, aims to systematically evaluate the performance of various TEGs under controlled conditions. This involves using a thermal plate device to emulate different temperature gradients, according with those measured before, and measure the corresponding electrical output. Understanding the electrical characteristics, such as voltage, current, and power output, under varying conditions, will provide crucial insights into selecting suitable TEGs for specific applications.

The third objective involves the in-situ characterization of the electrical energy output of TEGs. This step entails deploying TEGs either in situ, in the identified thermal hot and cold spots within the building, or in the identified items but tested at the lab. The aim is to evaluate the effectiveness of TEGs in generating electrical power within indoor environments. The study will assess the overall energy output of TEGs in practical applications. This will help determine the feasibility of using a TEG as a sustainable power source for indoor IoT sensor nodes, addressing any operational challenges that may arise.

In summary, this project, as part of the SUSTAIN project's Work Package 5 (WP5), aims to explore the potential of TEGs as a sustainable and autonomous power source for indoor IoT sensor nodes. By conducting a comprehensive study that includes thermal mapping, laboratory characterization, and in-situ testing, we aim to provide valuable insights into the practical application of TEGs in real-world indoor environments. The findings of this study could significantly contribute to the development of more sustainable IoT systems, reducing reliance on conventional batteries and minimizing environmental impact.

2 Temperature measurement of heat and cold sources across the building

2.1 Introduction

Buildings contribute significantly to global energy consumption due to the presence of numerous components and devices which often produce waste heat as a by-product of their normal functions. Utilizing this waste heat can enhance energy efficiency and sustainability by allowing sensors to function autonomously and deliver crucial data without relying on external power sources. Potential thermal sources in a building are different kinds of lamps, which also generate heat, and the water pipes of an HVAC system. In addition, battery chargers of mobile devices, e.g. laptops, also generate heat when charging. Finally, metallic objects, such as window frames, can exhibit important temperature variations when exposed to direct sunlight. In this section, several of these objects and items present at our School are assessed by measuring their temperature.

2.2 Materials and Methods

Measurements have been carried out at the Castelldefels School of Telecommunications and Aerospace Engineering (EETAC) from Universitat Politècnica de Catalunya (UPC). The school is located within the Mediterranean Technology Park in Castelldefels, which is at around 20 km from the centre of Barcelona (Catalonia, Spain).

Thermal Energy Sources

This study focuses on several thermal energy sources which can be found at the School: Linear Fluorescent Lamps (Linear FL), Compact Fluorescent Lamps (CFL), Light Emitting Diode (LED) Lamps, a Battery Laptop Charger, Hot and Cold Water Pipes, and Window Frames. Each of these sources presents unique opportunities and challenges for thermal energy recovery and conversion. Fig. 4 illustrates the various thermal energy sources explored in this study, which are described below.



Figure 4. Potential indoor thermal energy sources

1. Linear FL: G13 18 W OSRAM Cool Daylight lamp.
2. CFL: Two 26 W OSRAM lamps within a housing (Staff Iberica SA, model no. 770811)
3. LED lamp: Simon Downlight 725.28 3000K, paired with a 20 W Eaglerise LS-20-550 LI controller.
4. Battery laptop charger.
5. Hot/Cold water pipes from the HVAC system.
6. Window frames.

Tested items 2 and 3 are the same found at our School (in corridors, classrooms, and laboratories) but a different model has been used for item 1. Hot and cold water pipes work during cold and hot seasons, respectively. The tested pipes are located within a room in the basement of the School. Metallic window frames are present in every room of the School. This study specifically examines a window frame in our research laboratory (C4-101). The battery laptop charger is the 65 W charger coming with a laptop (Acer TravelMate P216-51) available at our lab.

Instrumentation and testing conditions

Linear FL and CFL are generally housed in metallic casings, while LED lamps are typically enclosed in plastic materials. Temperature measurements for Linear FL and CFL were taken on their metallic housings, rather than directly on the lamps themselves. For the LED lamp, the measurements were conducted on the box enclosure of the electronic controller. It is important to note that the lamps were not measured in their actual installed positions but instead taken to our lab. In contrast, for battery laptop charger, hot and cold pipes, and window frame, the temperature measurements were taken directly on the surface of the objects and in their actual installed positions.

This study utilizes at least two Pt100 sensors: one to measure the temperature of the object and another to measure the ambient temperature. In some cases, several sensors were first used to locate the hottest spot of the item. For instance, in the CFL, four sensors were used: one for the ambient temperature and the remaining three positioned on the metallic parts. Fig. 5 illustrates the final locations, indicating the hottest points on each object. A thermal paste (RS PRO 707-4736) was used to improve the thermal contact of the sensors with the objects and the sensors were fixed with tape. In addition, the thermal insulator material covering the pipes was sliced to direct contact the sensors with the pipes.



Figure 5. Hot spot where temperature recorded for each object

The Pt100 wire terminals were connected to the DAQ (Keysight DAQ970A), which was monitored and controlled via a computer running LabVIEW software. All the temperature data were subsequently recorded and stored in an Excel file for further analysis.

2.3 Experimental Results and Discussion

As an example, Fig. 6 shows the (a) measurement setup and (b) temperature data record for the water pipes conducted over a period of 5 days, from April 18 to April 22, 2024. During this time, only the hot pipe was active, while the cold pipe remained off. So, the data just correspond to the hot pipe and to the ambient temperatures. They reveal that the hot pipe is active during school hours, approximately from 8 AM to 8 PM, and is inactive during the weekend (20 and 21 April). When active, the hot pipe reaches an average temperature of 60 °C. Fig. 7 displays the measurement setup and temperature data record for the Linear FL. Unlike the piping system, this measurement was conducted over a shorter duration of 11 hours. The results indicate that the temperature of the Linear FL stabilized within a 0.6 °C band after approximately 3 hours of operation, maintaining a consistent temperature as long as the lamp remained on. During this condition, the surface temperature averaged around 50 °C. Similar methods were applied to other objects, with temperature measurements taken over specific periods and averages recorded once stability was reached. Table 1 presents summarized results for all the cases, where T_H is the object temperature and T_L is the ambient temperature.

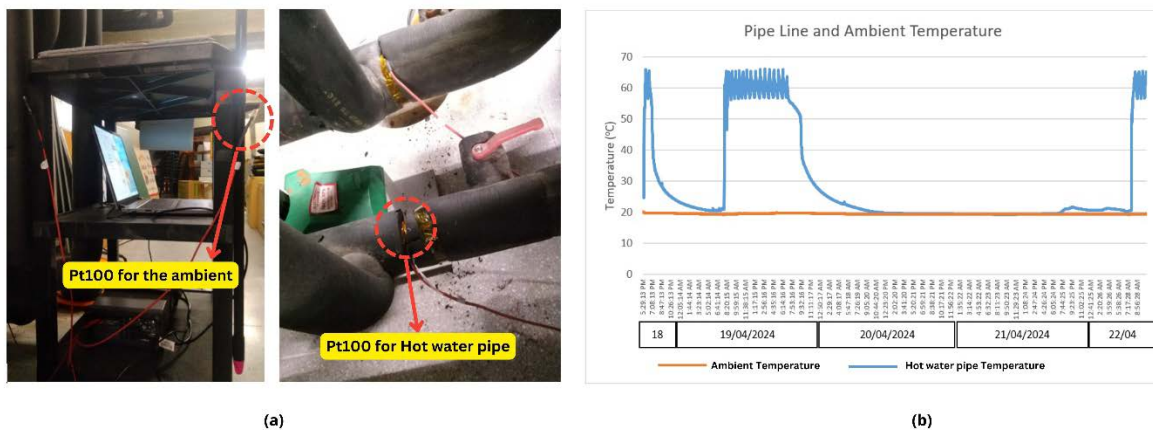


Figure 6. (a) Measurement setup and (b) temperature data record for the pipes.

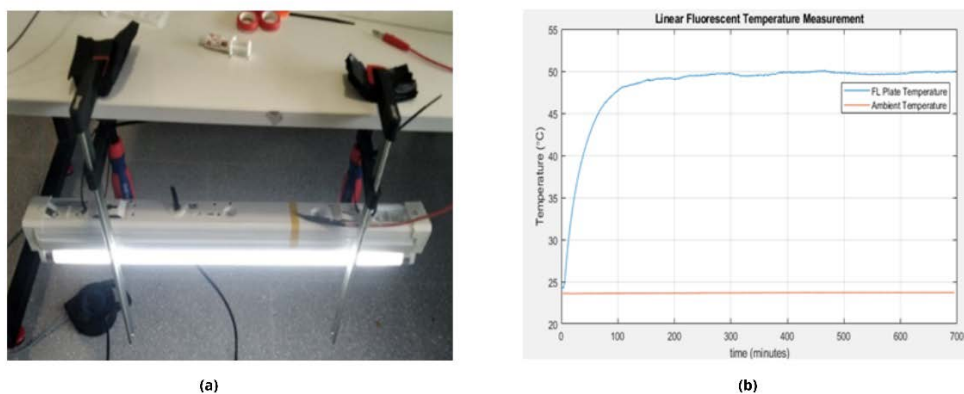


Figure 7. (a) Measurement setup and (b) temperature data record for the Linear FL.

Table 1. Temperatures for the different items, also including the ambient and differential temperatures

Objects	T_L (°C)	T_H (°C)	ΔT (°C)
Linear FL	23.7	49.9	26.2
CFL	26.2	57.8	31.6
LED	26.7	55.6	28.9
Battery Laptop Charger	25.8	57.3	31.5
Hot Pipe	19.7	59.8	40.1
Cold Pipe	23.7	12.3	-11.4
Window Frame	23.7	34.2	10.5

For the Linear FL, CFL, and LED lamps, the temperatures of ΔT remain relatively constant at the values shown in Table 1 as long as the devices are powered ON. For the battery laptop charger, the data recorded in Table 1 reflects the highest value of ΔT observed during the charging process while the laptop was ON. This peak occurred when the battery reached approximately 60 % of its charging state. When the battery was fully charged, ΔT decreased to around 40 °C. For the cold pipe, measurements were performed when it was operative, specifically on July 19th, 2024, from 1 PM to 3 PM. Here, the temperature was lower than the ambient, resulting in negative values of ΔT . In the case of window frame, the values in Table 1 reflect the temperature measured on the indoor-facing side of the frame when the window was directly exposed to direct sunlight. The measurement of the window frame was conducted on May 5, 2024, with peak temperature values recorded between approximately 5:10 PM and 5:45 PM. Of course, when the frame is not exposed to direct sunlight, such as in the morning or during the night, ΔT is significantly lower, around 2 to 3 °C in the morning and dropping to less than 1 °C during midnight.

Discussion

The substantial temperature differences observed in the monitored objects present significant opportunities for powering IoT nodes. Each object, as documented before, generates relatively high temperatures, resulting in a notable ΔT of more than 10 °C. These temperature gradients are crucial for effective thermal energy harvesting, as they create the necessary conditions for thermoelectric generation. Fig. 8 shows the summary results of ΔT for the tested objects.

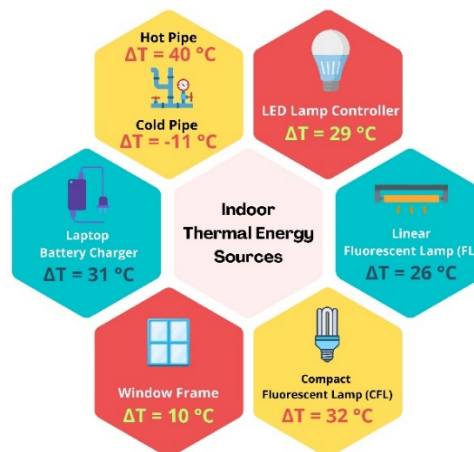


Figure 8. ΔT for the tested objects and items

This potential for power generation highlights the viability of using TEGs in capturing and converting waste heat into usable electrical energy. This approach to energy harvesting is particularly advantageous for powering indoor autonomous sensors, enabling them to function independently by harnessing the thermal energy present in common building elements including artificial lamps, device chargers, hot/cold water piping systems and window frames. The integration of TEGs with these thermal sources could contribute to more sustainable energy practices by reducing reliance on external power sources for powering autonomous sensor nodes.

3 Laboratory characterization of commercial TEGs using a thermal plate

3.1 Introduction

The laboratory characterization of commercial TEGs is an essential step in understanding their performance and suitability for specific applications. This phase involves a series of controlled experiments designed to systematically evaluate the electrical output of a couple of commercial TEG models with three different heatsinks and under different temperature gradients, which emulate those found in Section 2. The TEG models were selected based on their availability and specifications. Relevant specifications are the Seebeck coefficient and the power factor.

The experimental setup involves a thermal plate device capable of precisely controlling and maintaining temperature on the hot side of the TEGs (T_H) to emulate the temperature gradients (ΔT) found in Section 2. Thus, the voltage, current, and power output of the TEGs were measured. This controlled environment ensures the repeatability and accuracy of the measurements, providing reliable data on the performance characteristics of each TEG.

Furthermore, the study investigates the impact of heatsinks on the overall performance of TEGs since effective thermal management is essential to maximize the temperature differential across the TEGs and enhance their power output. The use of high-conductivity thermal interface materials and efficient heatsinks can significantly improve the energy harvesting capability of TEGs. By optimizing these components, the study aims to develop the effective integration of TEGs into indoor environments to maximize the electric power output.

3.2 Materials and Methods

Testing setup

For the purpose of characterization of commercial TEGs, our study employs a thermal plate (QInstruments ColdPlate 2016-0110), Pt100 sensors, a DAQ (Keysight DAQ970A), and Source Measure Unit (SMU, Keysight B2901A). The thermal plate, DAQ and SMU were connected via USB to a computer, which controlled them. Fig. 9 illustrates the complete setup.

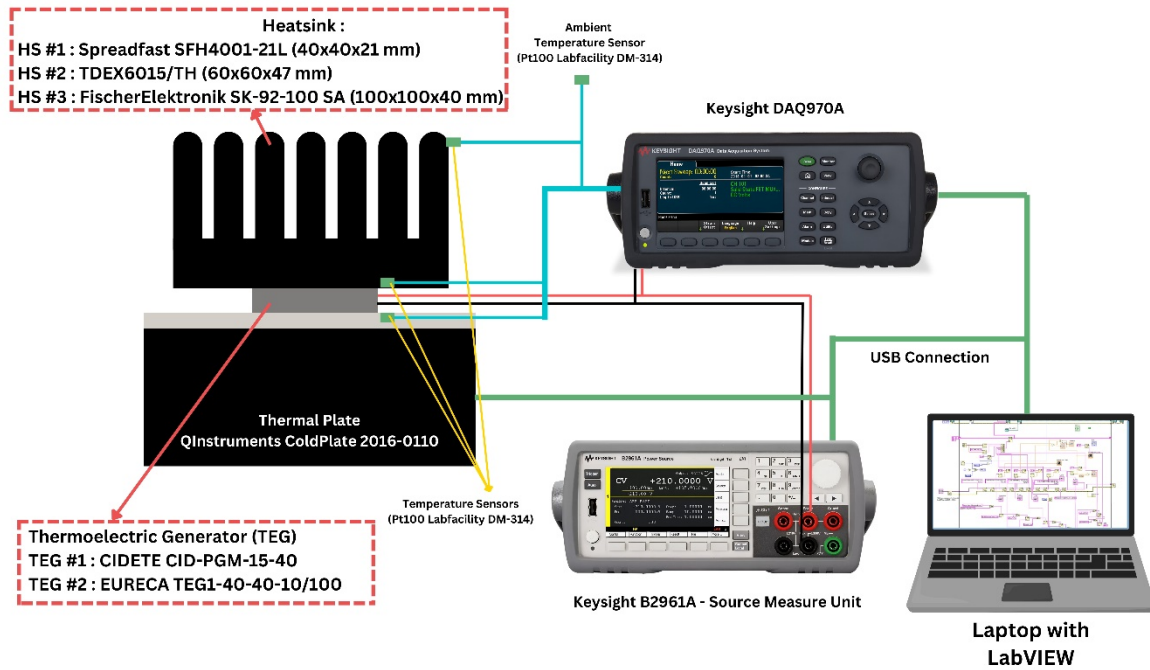


Figure 9. Experimental setup for the lab characterization of the TEGs using a thermal plate

This study utilized four Pt100 sensors to measure temperatures at multiple points: the thermal plate (as the hot side of the TEG, T_H), the bottom surface of the heatsink (as the cold side of the TEG, T_C), the top fin of the heatsink, and the ambient environment (T_L). The Pt100 sensors were connected to a DAQ, along with the TEG output, allowing the DAQ to simultaneously record temperature and V_{OC} using its 20-channel multiplexer feature. The thermal plate was controlled and monitored via a laptop running QCom software, a software from its manufacturer, which allowed setting the thermal plate temperature.

For the characterization of the TEG, an SMU was used, utilizing its sweep function to obtain the current-voltage (I-V) characteristics, while the power of the TEG was calculated using

$$P = V \times I \quad (7)$$

where P , V , and I are output power, voltage and current of the TEG, respectively. Once the temperature of the heatsink fin stabilized, defined as a fluctuation of less than 0.2 °C for over one minute, the SMU was activated. The previous DAQ V_{OC} reading served as a reference for the SMU to perform the voltage sweep function, ranging from 0 to V_{OC} , in 100 equal steps. When the voltage sweep was set to 0, it simulated a load of 0 Ω , creating a short circuit condition. This resulted in the measurement of the short circuit current (I_{SC}). Both the DAQ and SMU were controlled and monitored through LabVIEW software, and all data were logged and saved in an Excel file for further analysis.

TEGs under test

Two TEGs were used: CIDETE CID-PGM-15-40 (TEG #1) and EURECA TEG1-40-40-10/100 (TEG #2) which have the same surface area, 40 x 40 mm². Table 2 shows detailed specifications of both TEGs.

Table 2. TEG specifications

Parameters	TEG #1	TEG #2
Physical Properties		
Width & Length, mm	40	40
Thickness, mm	3.15	3.2
Thermal Properties		
Max Hot Side Temperature, °C	220	120
Max Cold Side Temperature, °C	50	-
Thermal conductivity, W/K	2.3	1.6
Seebeck coefficient, mV/K	66	82
Electric Properties		
	$\Delta T = 170\text{ }^{\circ}\text{C}$	$\Delta T = 100\text{ }^{\circ}\text{C}$
Power, W	10.85	10
Opened Circuit Voltage, V	11.2	8.2
Internal Resistance, Ω	2.84	1.7

Heatsinks under test

The TEGs were tested with the integration of a heatsink in the cold side for effective thermal management. The heatsinks used in this study are Spreadfast SFH4001-21L (HS #1), TDEX6015/TH (HS #2), and FischerElektronik SK-92-100 SA (HS #3), which present different base sizes, with HS #1 the smallest and HS #3 the largest. Table 3 and Fig. 10 show the specifications and pictures of the heatsinks, respectively.

Table 3. Heatsink specifications

Parameters	HS #1	HS #2	HS #3
Width (mm)	40	60	100
Length (mm)	40	60	100
Height (mm)	21	47	40
Thermal Resistance ($^{\circ}\text{C}/\text{W}$)	2.2 – 1.1 ^{*)}	0.5 ^{**)}	2.1 - 0.9 ^{**)}

^{*)} The thermal resistance is in accordance with an air flow range of 200 to 800 linear feet per minute (LFM).

^{**)} The thermal resistance is not specified with regard to whether it is under natural or forced convection conditions.

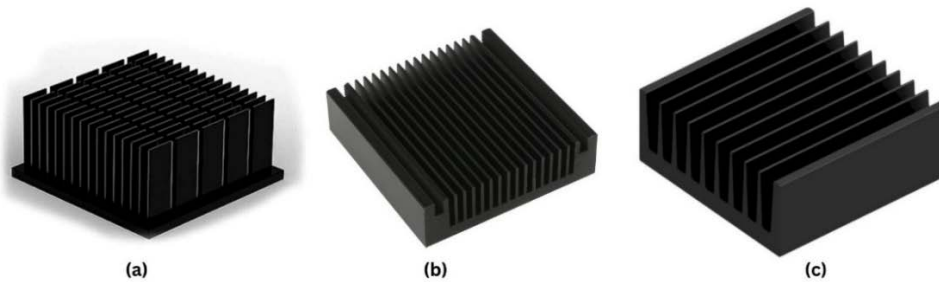


Figure 10. Picture of the heatsinks used in this study: (a) HS #1 (b) HS #2 (c) HS #3

Testing method

The testing method involves a detailed protocol to systematically evaluate the electrical output of the TEGs under controlled temperature conditions. Six different combinations were tested corresponding to the two TEGs and three heatsinks. High-conductivity thermal paste was used between the TEG and both the thermal plate and the heatsink, which was completely renewed each time the heatsink was changed to ensure consistent coverage across all contact surfaces for efficient heat transfer. The thermal plate was programmed to establish specific temperature differentials (ΔT) between the plate (T_H) and the ambient environment (T_L), from 5 °C to 40 °C in steps of 5 °C. In another scenario, we also investigated negative temperature gradients to emulate the case of the cold pipe, setting ΔT from -5 °C to -20 °C in steps of 5 °C.

In the experiments, ΔT_{TEG} was not measured exactly, since the temperature sensors for T_H and T_C were placed on a position which also includes the thermal interface materials, as illustrated in Fig. 11. We refer to this measurement as $\Delta T'_{TEG}$ which is calculated as

$$\Delta T = T_H - T_C \quad (8)$$

where

$$\Delta T'_{TEG} = \left(\frac{R_{TEG} + 2R_{TIM}}{R_T} \right) \Delta T = \left(1 + \frac{2R_{TIM}}{R_{TEG}} \right) \Delta T_{TEG} \quad (9)$$

So, $\Delta T'_{TEG} > \Delta T_{TEG}$.

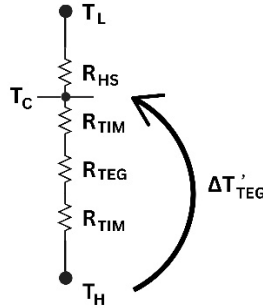


Figure 11. Hot side and cold side of TEG measurements

Eq. (1) and (3) can be reformulated in function of $\Delta T'_{TEG}$ as

$$V_{OC} = S \Delta T'_{TEG} \left(\frac{R_{TEG}}{R_{TEG} + 2R_{TIM}} \right) \quad (10)$$

$$P_{MPP} = \frac{V_{OC}^2}{4R_L} = \frac{S^2 (\Delta T'_{TEG})^2}{4R_L} \left(\frac{R_{TEG}}{R_{TEG} + 2R_{TIM}} \right)^2 \quad (11)$$

which are proportional to $\Delta T'_{TEG}$ and its square, respectively.

3.3 Experimental Results and Discussion

The six combinations of TEGs and heatsinks are assessed in terms of open circuit voltage (V_{OC}), short circuit current (I_{SC}), and maximum power output (P_{MPP}) across varying temperature differences (ΔT). The section provides a comprehensive analysis of the data, highlighting trends, comparing performances, and offering recommendations for optimal configurations and future work.

Experiments with $\Delta T > 0$ °C

TEG #1

Fig. 12, 13, 14, represent the experimental power-voltage characteristic of TEG #1 paired with HS #1, HS #2, and HS #3, respectively. In addition, the maximum power points (P_{MPP}) are highlighted through a dashed black line. The graphs show the behaviour predicted in Fig. 2, with P_{MPP} also located around $V_{oc}/2$. The results demonstrate that the combination of TEG #1 with HS #3 exhibits better performance, evidenced by its higher P_{MPP} in comparison to the other heatsink combinations. This is coherent with the expressions of Section 1.1. A larger heatsink leads to a lower R_{HS} and, thus, from (6) to a higher value of ΔT_{TEG} , which from (3) leads to a larger P_{MPP} . However, this combination requires a considerable amount of space due to the size of the heatsink, which can be unfeasible in space-restricted scenarios.

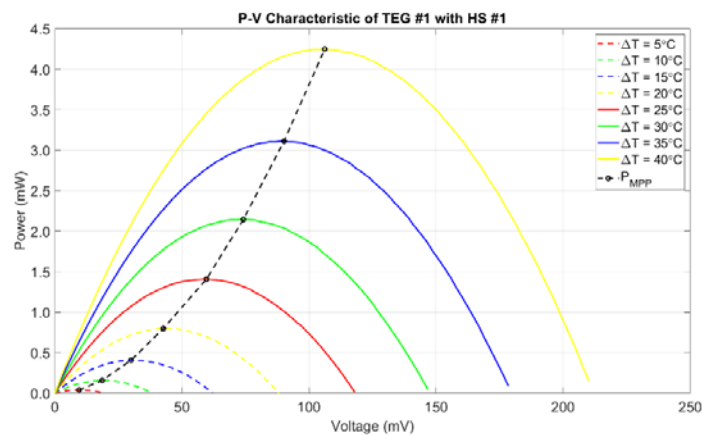


Figure 12. P-V characteristic of TEG #1 with HS #1

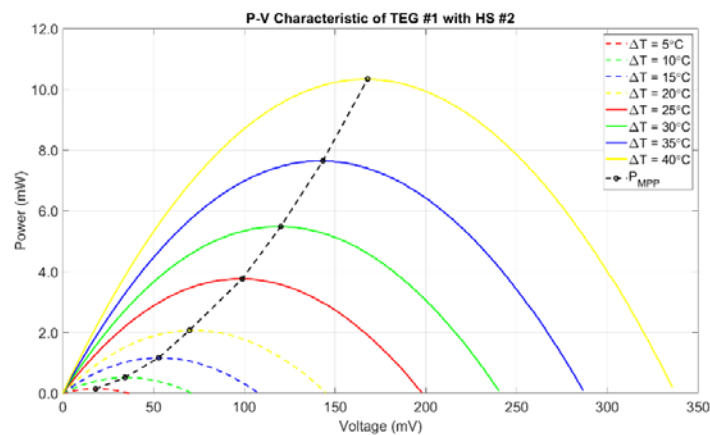


Figure 13. P-V characteristic of TEG #1 with HS #2

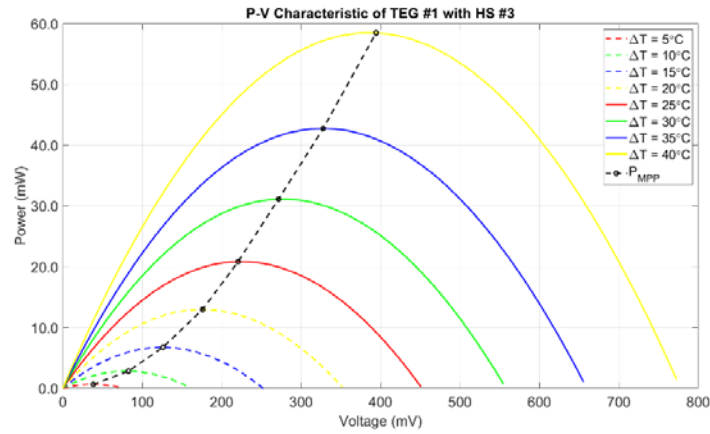


Figure 14. P-V characteristic of TEG #1 with HS #3

Tables 4, 5, 6 provide the values of V_{OC} and P_{MPP} corresponding to Figures 12, 13, 14, respectively. Apart, measured temperatures and I_{sc} are also provided. As can be seen, $\Delta T'_{TEG}$ is just a fraction of the overall ΔT , which agrees with (9). For each table, V_{OC} increases nearly proportionally to $\Delta T'_{TEG}$, as predicted by (10). For example, in Table 4, V_{OC} is 19.3 mV when $\Delta T'_{TEG}$ is 0.5 °C, nearly doubling to 38.1 mV when $\Delta T'_{TEG}$ approximately doubles to 1.1 °C. In addition, P_{MPP} nearly increases with the square of $\Delta T'_{TEG}$, as predicted by (11). On the other hand, $\Delta T'_{TEG}$ increases from HS #1 to HS #3, in agreement with (9), since R_{HS} becomes lower for larger heatsinks. However, it is observed that $\Delta T'_{TEG}$ just slightly increases from Table 4 to Table 5 whereas the increase of V_{oc} is relatively much larger. So, there is not a linear relationship, which seems in contradiction with (10). One explanation can be that the TIM material (from both sides of the TEG) is renewed when changing the heatsink, which can lead to different values of R_{TIM} for each combination. A lower R_{TIM} for the case of HS #2 with respect to HS #1 can lead to a significant increase of V_{oc} even for similar values of $\Delta T'_{TEG}$. Anyhow, this hypothesis must be further investigated. For HS #3 both $\Delta T'_{TEG}$ and V_{oc} significantly increase with respect HS #2, which can be justified by a lower R_{HS} .

Table 4. Experimental data for TEG #1 with HS #1

ΔT (°C)	T_H (°C)	T_C (°C)	$\Delta T'_{TEG}$ (°C)	V_{OC} (mV)	I_{SC} (mA)	P_{MPP} (mW)
5	30.3	29.8	0.5	19.3	8.8	0.041
10	35.7	34.6	1.1	38.1	16.7	0.16
15	41.1	39.3	1.8	62.0	26.6	0.41
20	46.2	43.8	2.5	88.3	36.8	0.79
25	51.5	48.3	3.3	118.0	48.3	1.41
30	56.6	52.5	4.1	146.8	59.0	2.14
35	61.7	56.8	4.9	178.5	70.30	3.11
40	66.4	60.9	5.5	210.2	81.3	4.25

Table 5. Experimental data for TEG #1 with HS #2

ΔT (°C)	T_H (°C)	T_C (°C)	$\Delta T'_{TEG}$ (°C)	V_{OC} (mV)	I_{SC} (mA)	P_{MPP} (mW)
5	31.5	30.9	0.6	36.6	15.8	0.14
10	36.5	35.4	1.2	70.9	30.0	0.52
15	41.6	39.8	1.8	107.9	44.5	1.17
20	46.6	44.2	2.4	144.9	58.8	2.07
25	51.5	48.3	3.3	197.8	78.4	3.77
30	56.2	52.0	4.2	240.2	93.8	5.49
35	61.1	56.1	5.0	286.6	109.6	7.65
40	66.0	60.2	5.8	335.8	126.3	10.34

Table 6. Experimental data for TEG #1 with HS #3

ΔT (°C)	T_H (°C)	T_C (°C)	$\Delta T'_{TEG}$ (°C)	V_{OC} (mV)	I_{SC} (mA)	P_{MPP} (mW)
5	30.2	28.5	1.8	76.1	34.5	0.64
10	35.6	32.0	3.6	160.3	70.9	2.82
15	40.9	35.4	5.5	252.1	108.5	6.73
20	46.2	38.6	7.5	352.0	149.1	12.95
25	51.2	41.8	9.5	450.9	187.4	20.84
30	56.4	44.9	11.4	554.7	226.8	31.12
35	61.3	48.0	13.3	655.5	263.5	42.74
40	65.7	50.3	15.4	772.8	306.0	58.50

TEG #2

Fig. 15, 16, 17 represent the experimental power-voltage characteristic of TEG #2 paired with HS #1, HS #2, and HS #3, respectively. On the other hand, Tables 7, 8, 9 provide the experimental data of different parameters. As with TEG #1, results show that HS #3 provides the highest values of P_{MPP} . However, TEG #2 provides lower values of P_{MPP} than TEG #1 in all cases (even it has a higher Seebeck coefficient, see Table 2), which is justified from the lower values $\Delta T'_{TEG}$ (roughly half).

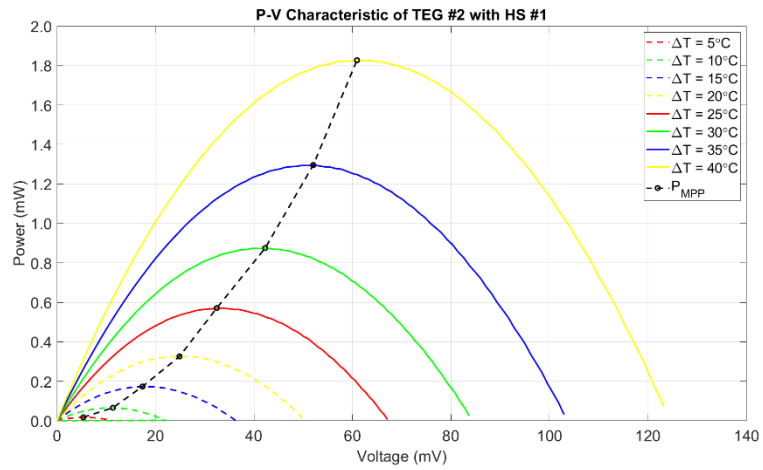


Figure 15. P-V characteristic of TEG #2 with HS #1

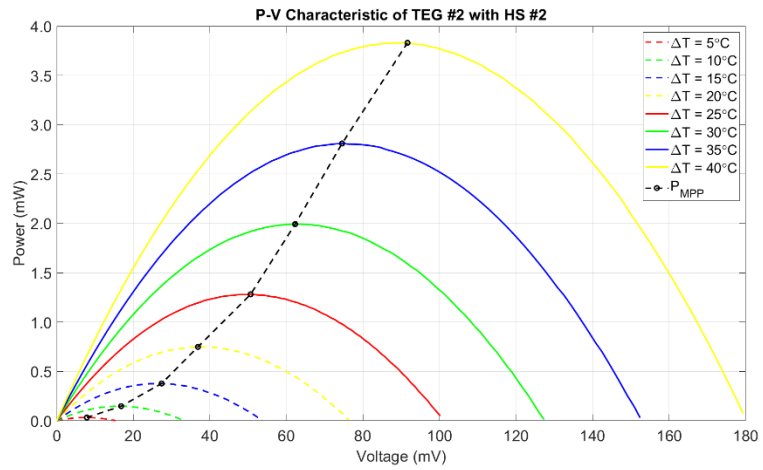


Figure 16. P-V characteristic of TEG #2 with HS #2

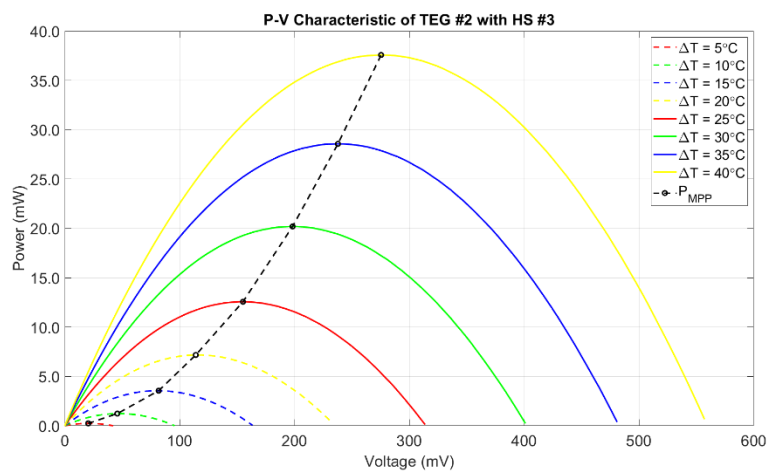


Figure 17. P-V characteristic of TEG #2 with HS #3

Table 7. Experimental data for TEG #2 with HS #1

ΔT (°C)	T_H (°C)	T_C (°C)	$\Delta T'_{TEG}$ (°C)	V_{OC} (mV)	I_{SC} (mA)	P_{MPP} (mW)
5	29.9	29.7	0.3	11.3	6.4	0.018
10	35.0	34.4	0.5	22.0	12.3	0.066
15	40.1	39.2	0.9	36.4	19.8	0.17
20	45.2	43.9	1.3	50.3	26.8	0.33
25	50.2	48.5	1.6	70.1	35.1	0.57
30	55.0	53.1	1.9	83.7	43.0	0.87
35	59.8	57.6	2.1	103.0	51.8	1.29
40	64.5	62.1	2.4	124.5	60.9	1.83

Table 8. Experimental data for TEG #2 with HS #2

ΔT (°C)	T_H (°C)	T_C (°C)	$\Delta T'_{TEG}$ (°C)	V_{OC} (mV)	I_{SC} (mA)	P_{MPP} (mW)
5	31.2	31.0	0.2	15.4	8.8	0.033
10	36.2	35.8	0.4	33.3	18.4	0.15
15	41.1	40.5	0.7	53.6	29.1	0.38
20	46.1	45.2	0.9	76.3	40.5	0.75
25	50.4	48.9	1.5	101.3	52.6	1.29
30	55.4	53.7	1.7	127.3	64.8	1.99
35	60.2	58.2	1.9	152.4	76.2	2.81
40	64.9	62.8	2.1	179.4	88.1	3.83

Table 9. Experimental data for TEG #2 with HS #2

ΔT (°C)	T_H (°C)	T_C (°C)	$\Delta T'_{TEG}$ (°C)	V_{OC} (mV)	I_{SC} (mA)	P_{MPP} (mW)
5	29.4	28.5	0.8	42.3	24.1	0.24
10	34.7	32.7	2.0	95.7	53.5	1.24
15	40.0	36.7	3.4	163.6	89.9	3.56
20	45.1	40.2	4.8	233.3	126.6	7.18
25	50.1	43.8	6.3	313.8	166.1	12.57
30	55.1	47.2	8.0	401.1	208.7	20.20
35	59.9	50.5	9.4	481.0	246.1	28.57
40	65.9	55.0	11.0	557.1	279.2	37.58

Experiment with $\Delta T < 0$ °C

In this setup, just the combination with the higher value of P_{MPP} for $\Delta T < 0$ °C was chosen, TEG #1 paired with HS #3. Since the thermal plate was colder than the ambient temperature, the TEG was reversed, thermally connecting the cold side to the thermal plate and the hot side to the heatsink. Fig. 19 shows the P-V graph whereas Table 10 shows the experimental data of different parameters.

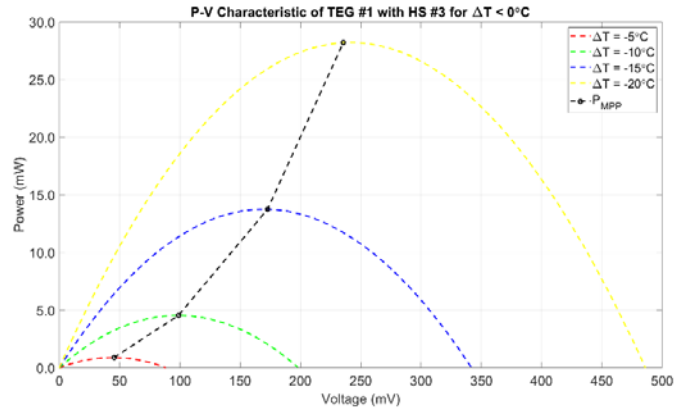


Figure 18. P-V characteristic of TEG #2 with HS #3 for $\Delta T < 0^\circ\text{C}$

Table 10. In-Lab characterization measurement of TEG #1 with HS #3 for $\Delta T < 0^\circ\text{C}$

ΔT ($^\circ\text{C}$)	T_H ($^\circ\text{C}$)	T_C ($^\circ\text{C}$)	$\Delta T'_{\text{TEG}}$ ($^\circ\text{C}$)	V_{OC} (mV)	I_{SC} (mA)	P_{MPP} (mW)
-5	19.0	21.0	-2.0	88.3	40.9	0.89
-10	13.7	18.2	-4.5	197.8	93.1	4.55
-15	8.4	16.2	-7.8	341.9	163.5	13.75
-20	3.5	14.6	-11.1	486.0	236.0	28.21

When ΔT was decreases to -20°C , P_{MPP} reaches 28.2 mW, which is more than double the value observed with the same combination for $\Delta T > 0^\circ\text{C}$ and at ΔT of 20°C . This is produced by a condensation effect, leading to the formation of dew on metal surfaces, including the heatsink, as illustrated in Fig. 18. So, water droplets cover the heatsink, which increase its thermal dissipation capability (reduction of R_{HS}). Thus, from (9), $\Delta T'_{\text{TEG}}$ increases, leading, from (10), to a higher V_{oc} and, from (11), to a higher P_{MPP} . This effect accentuates for larger value of $|\Delta T|$, i.e. R_{HS} keeps decreasing, which explains why $|\Delta T'_{\text{TEG}}|$ and V_{oc} more than linearly increase with $|\Delta T|$ and P_{MPP} more than increases with the square of $|\Delta T|$.

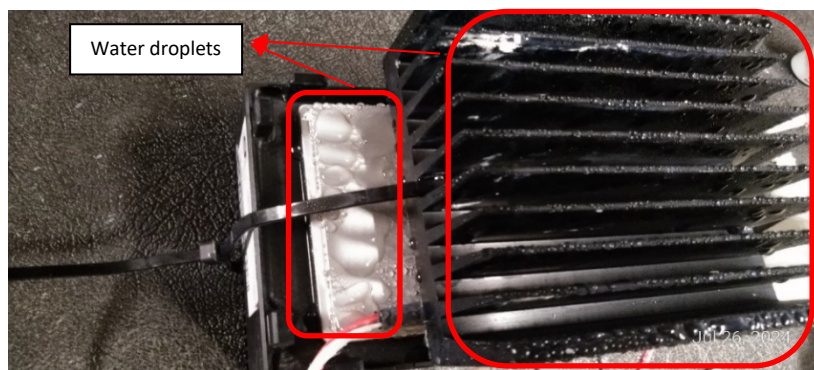


Figure 19. Water droplets on metal surfaces during condensation

Discussion

A heatsink plays a vital role in dissipating excess heat from the TEG. In this study, HS #3 demonstrated superior performance, because its larger size, compared to the other heatsinks, resulting in significantly

improved thermal dissipation. This allowed the TEG to achieve a higher electrical power output. However, this can be problematic in space-constrained situations. In addition, TEG #1 achieved a higher power output than TEG #2. Tables 11 and 12 summarize the results of P_{MPP} for ΔT minimum (5 °C) and maximum (40 °C) and the different combinations.

Table 11. P_{MPP} for $\Delta T = 5\text{ °C}$

Heatsinks	P_{MPP} (μW)	
	TEG #1	TEG #2
HS #1	41	18
HS #2	140	33
HS #3	640	240

Table 12. P_{MPP} for $\Delta T = 40\text{ °C}$

Heatsinks	P_{MPP} (mW)	
	TEG #1	TEG #2
HS #1	4.25	1.83
HS #2	10.34	3.83
HS #3	58.50	37.58

In cases where the temperature of the thermal source is below the ambient temperature, humidity becomes a critical factor to consider due to its impact on system performance. Specifically, when the temperature of the thermal source falls below the dew point of the surrounding air, condensation can occur, resulting in the formation of dew on the surface of metallic components, including heatsinks. This phenomenon reduces the thermal resistance of the heatsink, increasing the thermal gradient across the TEG. On the other hand, while dew formation on heatsinks can improve heat dissipation and overall system performance under certain conditions, it can also pose potential risks associated with corrosion and degrade performance. Table 13 summarizes the results for $\Delta T < 0\text{ °C}$.

Table 13. P_{MPP} for $\Delta T < 0\text{ °C}$ (TEG #1 with HS #3)

ΔT (°C)	P_{MPP} (mW)
-5	0.89
-10	4.55
-15	13.75
-20	28.21

4 In-situ building characterization of TEGs and their electrical energy output

4.1 Introduction

In-situ characterization is essential to understand the actual performance of TEGs when interacting with the thermal energy sources discussed in Section 2. By evaluating how TEGs perform under actual conditions, the optimal locations for installation can be identified, and realistic estimates of energy savings can be made. For instance, in-situ testing can determine if heat sources like hot water pipes or CFL lamps generate enough thermal energy for efficient TEG operation. Moreover, it offers insights into potential enhancements in TEG system design or installation methods, such as improving thermal contact or using specific materials, which can significantly boost energy conversion efficiency when integrated into complex building systems.

In Section 2, we have located and characterized several thermal sources and in section 3 we have characterized two TEGs with several heatsinks with a thermal plate emulating the thermal sources. In this section, the best combination of Section 3 (TEG #1 with HS #3) will be directly assessed with the thermal sources of Section 2. A remark has to be introduced, though. When the TEG is attached to the thermal source objects, the temperature differential ΔT can reduce with respect to those identified in Section 2. The reason for this drop is introduced by the internal thermal resistance of the thermal source objects and the TEG system. Fig. 20 illustrates this phenomenon. When TEG system is not attached, ΔT can be simply calculated as $T_H - T_L$. However, when TEG system is attached, a new temperature T'_H can be defined, which is given by

$$T'_H = \frac{R_T}{R_T + R_S} (T_H - T_L) + T_L \quad (12)$$

and R_S denotes the internal thermal resistance of the thermal source. R_S can arise from various heat transfer processes, such as radiation, which introduces radiative thermal resistance [12], and materials covering the thermal source. These materials, whether metallic or plastic, contribute to the R_S value, affecting the heat flow to the TEG system. Plastics exhibit higher thermal resistance compared to metals due to their significantly lower thermal conductivity [13], making them less efficient at transferring heat.

The effective ΔT is now calculated as $T'_H - T_L$, leading to a lower value than before and given by

$$\Delta T = T'_H - T_L = \frac{R_T}{R_T + R_S} (T_H - T_L) \quad (13)$$

which reduces for increasing values of R_S .

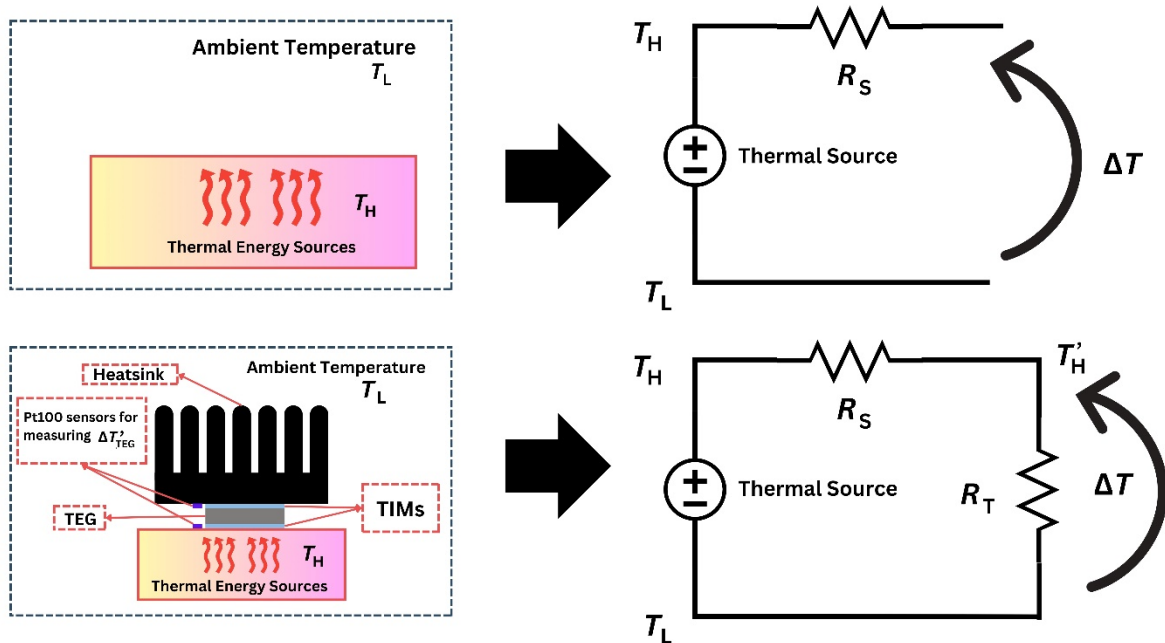


Figure 20. Illustration on thermal source before and after TEG system attachment

4.2 Materials and Methods

TEG and heatsink under test

Based on the results of Section 3, the combination of TEG #1 paired with HS #3, which provided the highest values of P_{MPP} , was chosen for the in-situ tests described in this Section.

Measurement setup

The experimental setup is the same than that of Fig. 9 but switching the thermal plate by the thermal sources of Section 2. Fig. 21 illustrates the attachment of the TEG system to the various thermal source objects. The TEG is optimally positioned at the hottest spot identified during the measurements in Section 2, allowing for maximum thermal energy capture and improved performance in converting heat to electrical power.



Figure 21. TEG system attachment to the various thermal source objects

Measurements were conducted between June and July (summer season), so the hot water pipe case was not tested since it was not in operation. Unlike the other cases, the piping system required an additional metallic component due to the non-flat surface of the pipe. This introduces extra thermal resistance from the metallic part and the thermal interface material, which can potentially reduce ΔT . Fig. 22 illustrates the setup for the cold pipe and its equivalent electrical model.

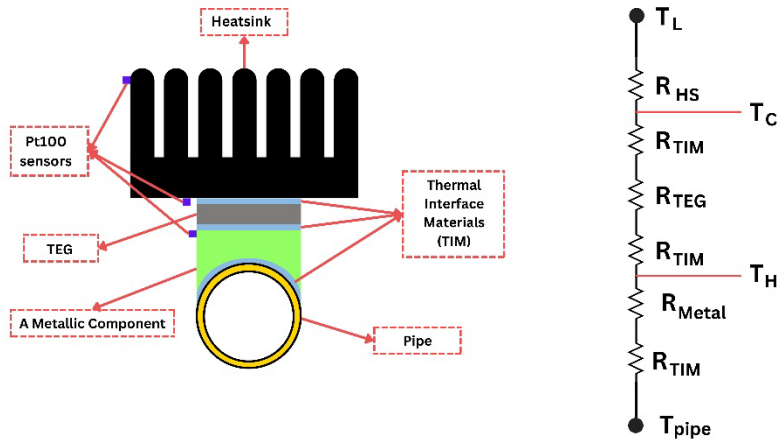


Figure 22. Measurement setup on piping system

Testing method The experiments utilized four Pt100 sensors. One was positioned on the object's surface, where the hot surface of the TEG was attached to measure T_H , as illustrated in Fig. 5. For the cold pipe, however, the sensor was attached to the top side of the metallic part, as illustrated in Fig. 22. Another sensor was placed on the bottom surface of the heatsink to measure T_C . The remaining two sensors were used to monitor the temperature at the top fin of the heatsink and the ambient environment (T_L). The testing methodology followed the same procedures outlined in Section 3. This approach was consistently applied to each heat source under investigation, ensuring a comprehensive evaluation of the TEG's performance across various real-world scenarios. The results from these tests provide valuable insights into the practical energy-harvesting capabilities of TEG #1 when paired with HS #3, particularly in relation to its integration with thermal energy sources.

4.3 Experimental Results and Discussion

Table 14 presents the results. The results indicate that the value of ΔT decreases with respect to those measured in Table 1, in Section 2, in accordance with the description of Section 4.1. In the case of Linear FL and CFL, heat is transferred from the heat source primarily through radiation, leading to a high internal thermal resistance in these objects. In Section 2, we observed ΔT values of 26 °C for the Linear FL and 32 °C for the CFL. However, once the TEG system was attached, ΔT significantly lowered to 15.6 °C for the Linear FL and slightly to 29.4 °C for the CFL. $\Delta T'_{TEG}$ of the Linear FL, shown in Table 14, was similar to that in Table 6 corresponding to $\Delta T = 15$ °C. For CFL, however, $\Delta T'_{TEG}$ in Table 14 was significantly decreased compared to that in Table 6 corresponding to the $\Delta T = 30$ °C. This discrepancy can be explained by the L-shaped design of the CFL cover and the relatively large size of the heatsink, as illustrated in Fig. 23. Heat was transferred to the heatsink not only from the hot side of the TEG but also from the metallic cover of the CFL. This additional heat transfer likely increases the heatsink temperature, resulting in a reduced value of $\Delta T'_{TEG}$. On the other hand, P_{MPP} values of the TEG, resulted from Linear FL and CFL, were coherent to the values shown in Table 6, for similar $\Delta T'_{TEG}$ values.

Table 14. Measurement results of TEG #1 attached on thermal source objects

Thermal Sources	T'_H (°C)	T_C (°C)	T_L (°C)	ΔT (°C)	$\Delta T'_{TEG}$ (°C)	V_{OC} (mV)	I_{SC} (mA)	P_{MPP} (mW)
Linear FL	39.3	34.6	23.7	15.6	4.7	218.2	94.1	5.06
CFL	58.7	53.0	29.3	29.4	5.8	272.5	109.4	7.36
LED Lamp	39.3	32.6	27.7	11.6	6.7	107.5	47.0	1.25
Battery Laptop Charger	42.6	32.2	26.4	16.2	10.4	189.1	82.0	3.83
Cold Pipe	19.0	14.1	23.5	-9.3	4.9	205.6	97.0	4.91
Window Frame	39.8	36.9	29.1	10.8	3.0	146.8	62.3	2.27

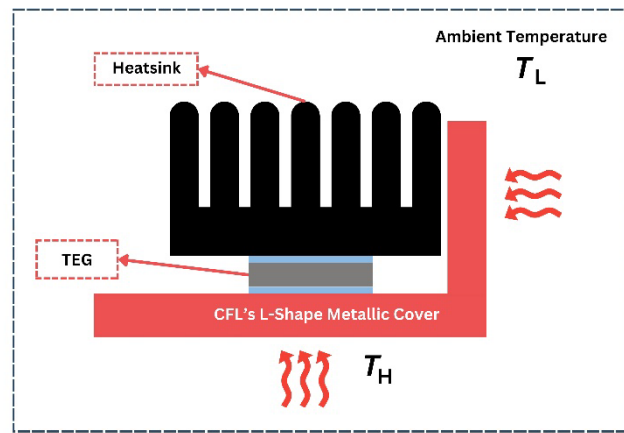


Figure 23. L-Shape metallic cover of CFL

In the case of LED lamp controller and the battery laptop charger, the values of ΔT , shown in Table 14, were also significantly lower than those measured in Table 1, in Section 2, i.e. 11.6 °C and 16.2 °C, respectively. Here, both the radiation heat transfer from the electronic components inside the enclosure box and the box plastic material were the cause, in accordance with the description in Section 4.1. However, the values of $\Delta T'_{TEG}$ in Table 14 were higher than those in Table 6 for similar values of ΔT . This could be attributed to a higher temperature at the measuring point of the thermal source (at the plastic box) with respect to the actual hot side of the TEG (as illustrated in Fig. 20) due to the limited heat transfer of the plastics material. As a consequence, the actual $\Delta T'_{TEG}$ would be lower than measured. This would also explain, in part, the lower values of P_{MPP} in Table 14 compared with those in Table 6. .

In the case of the cold pipe, ΔT was -9.3 °C, slightly reduced compared to the value in Table 1. On the other hand, $\Delta T'_{TEG}$ and P_{MPP} were similar to those of Table 10 with $\Delta T = -10$ °C. Finally, ΔT was 10.8 °C for the window frame, very similar to the value in Table 1. Here, $\Delta T'_{TEG}$ and P_{MPP} were slightly smaller than those of Table 6 with $\Delta T = 10$ °C. Due to its large size, the bottom surfaces of the heatsink were also hit by the sunlight, through the window glass, which could slightly increase the temperature of the heatsink, leading to lower $\Delta T'_{TEG}$ and P_{MPP} .

Discussion

In-situ testing occurs in real-world conditions, where several factors can affect heat transfer efficiency. One key factor is internal thermal resistance, which arises from the type of heat transfer and the materials to which the TEG is attached. For instance, conduction through different materials can introduce thermal resistance that impedes effective heat flow, while radiation can lead to an increase in thermal resistance. Additionally, factors like surface roughness and material properties can further influence thermal contact and transfer efficiency. These conditions often lead to reduced temperature differentials across the TEG, ultimately impacting its power output. Fig. 24 presents the maximum power output of TEG #1 with HS #3, summarizing the in-situ testing results across various thermal energy sources.

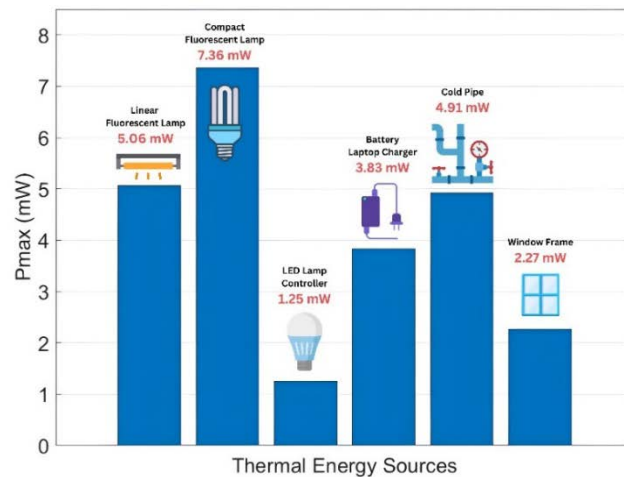


Figure 24. Maximum power output of TEG #1 with HS #3 across various thermal energy sources

As a result, the highest P_{MPP} (7.36 mW) resulted when the TEG was attached to the CFL and the lowest (1.25 mW) when attached to the LED lamp controller. Each object has different characteristics and challenges. Understanding these real-world challenges is essential for optimizing TEG installations in practical applications. Addressing issues like thermal contact quality and ensuring uniform heating could help enhance energy capture, thus improving the overall efficiency of thermal energy harvesting systems in building environments. Furthermore, strategically positioning TEGs can enhance energy capture by allowing the system to respond more effectively to changing thermal conditions. By addressing these challenges, we can enhance the overall efficiency of thermal energy harvesting systems in building environments, making them more viable for powering autonomous sensors and contributing to sustainable energy management practices.

5 Conclusions

The thermal measurement conducted across various locations in the building identified several potential thermal energy sources, such as Linear FL, CFL, LED lamps, battery laptop chargers, hot and cold pipes, and window frames. These objects offer promising ΔT values ranging from 10 °C to 40 °C, making them well-suited for thermoelectric power generation. This study emphasized the necessity of understanding the thermal dynamics of each potential source and the impact of material properties on heat transfer, which are critical factors in the practical deployment of TEGs within a building environment.

This study involved laboratory characterization of commercial TEGs, temperature measurements of heat and cold sources within the building, and in-situ evaluation of TEG performance. The controlled thermal gradients in the lab enabled an accurate assessment of power output, particularly for TEG #1 and TEG #2, when paired with HS #1, HS #2, and HS #3. The findings revealed that HS #3 provided superior thermal management for both TEGs compared to the other heatsinks, with TEG #1 demonstrating better performance than TEG #2. Paired with HS #3, at ΔT 5 °C P_{MPP} of TEG #1 reached 0.64 mW, while TEG #2 produced 0.24 mW. When ΔT increased to 40 °C, TEG #1 reached P_{MPP} of 58.50 mW, whereas TEG #2 reached 37.58 mW. When the temperature difference was set to a negative value, water droplets formed on the heatsink surface due to the thermal plate being below the ambient dew point, enhancing heat dissipation effectiveness. However, it is important to closely monitor and manage humidity levels to prevent potential issues related to corrosion and system instability in the future.

In-situ testing takes place under real-world conditions, where various factors can significantly influence heat transfer efficiency. One of the main factors is internal thermal resistance of the thermal sources, which results from the type of heat transfer and the materials to which the TEG is connected. For example, radiative heat transfer may also increase the internal thermal resistance of the heat source. Furthermore, the texture of surfaces and the fundamental properties of the materials can have a substantial impact on thermal contact and transfer efficiency. These real-world conditions frequently result in a decrease in ΔT when the TEG system is installed, consequently lowering its power output. Despite these challenges, the TEG can still generate P_{MPP} in the range of 1 to 8 mW, depending on the object to which it is attached. The largest P_{MPP} achieved was 7.36 mW when the TEG was attached to the CFL, and the smallest value was 1.25 mW when attached to the LED lamp controller. This power output demonstrates the device's capability to harness available thermal energy even under suboptimal conditions. The ability to produce electric power within this range is significant, as it can support various low-energy applications, particularly in powering indoor autonomous sensors.

6 References

- [1] Y. Lu, S. Papagiannidis, and E. Alamanos, "Internet of Things: A systematic review of the business literature from the user and organisational perspectives," *Technological Forecasting and Social Change*, vol. 136, pp. 285–297, Nov. 2018, doi: 10.1016/j.techfore.2018.01.022.
- [2] I. Mathews, S. N. Kantareddy, T. Buonassisi, and I. M. Peters, "Technology and Market Perspective for Indoor Photovoltaic Cells," *Joule*, vol. 3, no. 6, pp. 1415–1426, Jun. 2019, doi: 10.1016/j.joule.2019.03.026.
- [3] P. Fiorini, I. Doms, C. Van Hoof, and R. Vullers, "Micropower energy scavenging," in *ESSCIRC 2008 - 34th European Solid-State Circuits Conference*, Edinburgh, UK: IEEE, Sep. 2008, pp. 4–9. doi: 10.1109/ESSCIRC.2008.4681783.
- [4] G. Famitafreshi, M. S. Afaqui, and J. Melià-Seguí, "A Comprehensive Review on Energy Harvesting Integration in IoT Systems from MAC Layer Perspective: Challenges and Opportunities," *Sensors*, vol. 21, no. 9, p. 3097, Apr. 2021, doi: 10.3390/s21093097.
- [5] A. Chakraborty *et al.*, "Photovoltaics for indoor energy harvesting," *Nano Energy*, vol. 128, p. 109932, Sep. 2024, doi: 10.1016/j.nanoen.2024.109932.
- [6] C. Covaci and A. Gontean, "Piezoelectric Energy Harvesting Solutions: A Review," *Sensors*, vol. 20, no. 12, p. 3512, Jun. 2020, doi: 10.3390/s20123512.
- [7] N. A. Eltresy *et al.*, "Smart Home IoT System by Using RF Energy Harvesting," *Journal of Sensors*, vol. 2020, pp. 1–14, Dec. 2020, doi: 10.1155/2020/8828479.
- [8] R. Owczarczak, "Indoor thermal energy harvesting for battery-free IoT building applications," *ELECTROTECHNICAL REVIEW*, vol. 1, no. 3, pp. 134–138, Mar. 2023, doi: 10.15199/48.2023.03.23.
- [9] R. Aridi, J. Faraj, S. Ali, T. Lemenand, and M. Khaled, "Thermoelectric Power Generators: State-of-the-Art, Heat Recovery Method, and Challenges," *Electricity*, vol. 2, no. 3, pp. 359–386, Sep. 2021, doi: 10.3390/electricity2030022.
- [10] H. Jouhara *et al.*, "Thermoelectric generator (TEG) technologies and applications," *International Journal of Thermofluids*, vol. 9, p. 100063, Feb. 2021, doi: 10.1016/j.ijft.2021.100063.
- [11] G. Sung, D.-Y. Na, and S.-J. Yook, "Enhancement of the cooling performance of a pin fin heat sink based on the chimney effect using aluminum tape," *International Journal of Heat and Mass Transfer*, vol. 201, p. 123613, Feb. 2023, doi: 10.1016/j.ijheatmasstransfer.2022.123613.
- [12] R. Wyczółkowski, T. Wyleciał, and M. Gała, "The possibility of simplified modelling of radiation heat transfer within a steel porous charge," *MATEC Web Conf.*, vol. 240, p. 01037, 2018, doi: 10.1051/matecconf/201824001037.
- [13] H. Chen *et al.*, "Thermal conductivity of polymer-based composites: Fundamentals and applications," *Progress in Polymer Science*, vol. 59, pp. 41–85, Aug. 2016, doi: 10.1016/j.progpolymsci.2016.03.001.

